



H2020-ICT-2020-2 Grant agreement no: 101017274

DELIVERABLE 1.3

Final DARKO elastic manipulator

Dissemination Level: PUBLIC

Due date: month 36 (December 2023)

Deliverable type: Report

Lead beneficiary: TUM

1 Introduction

The Darko project aims to advance the frontier of agile production by realizing a new flexible and energy-efficient robot arm that is capable to tackle the distinct challenges associated with efficient intralogistics. In the proposal, we have identified throwing as a key manipulation strategy to achieve this goal [1]. Throwing considerably extends the work space of a robot since parts can be sorted without having to move the mobile base. Thus, the time and energy-efficiency of intralogistics could be significantly improved.

Endowing robots with this capability, however, comes with some difficult challenges in terms of hardware requirements due to the high speed gain that is necessary for successful throwing. State-of-the-art actuation technologies such as torque-controlled rigid joints are limited in speed, energy-efficiency and peak power [2]. If we take a look at the human musculoskeletal system, we notice that it performs much better in these areas. The key difference to rigidly actuated robots is intrinsic elasticity. There have been various efforts to exploit elasticity in the robotics community as well: *Series Elastic Actuation* (SEA, [3, 2]) and *Variable Stiffness Actuation* (VSA, [4, 5, 6]) are some notable examples.

SEAs are highly energy-efficient and capable of dynamic manoeuvres due to their ability to exploit their natural dynamics (storage and release of energy in springs). For speed maximization, they use a so-called resonant excitation strategy, i.e. a bang-bang-like signal to induce oscillations [2]. However, since the timing of energy storage and release cannot be controlled [7], employing a resonant excitation strategy results in a rather uncoordinated, haphazard swing-up motion.

Looking back at humans, we can observe a different strategy for speed maximization. We humans use a *proximo-distal sequence*: Each segment in the kinematic chain reaches its velocity maximum in sequential order. Hereby, the energy transfer from proximal to distal joints is maximized. For example, the wrist velocity (and thus the speed of the thrown object) is increased by braking the motion of the elbow which can be explained by conservation of momentum [1]. This phenomenon is also referred to as *inertia timing* [8]. VSAs can exploit a similar effect by approximate decoupling (i.e. setting the stiffness to its lowest value) [2]. Since a second motor for stiffness adaptation is necessary, the complexity of the resulting mechanism is greatly increased. From previous experience we know that these mechanisms can be quite bulky and thus might not meet the requirements of a compact and efficient design for the arm envisioned in Darko. Instead, we investigated how an SEA plus a suitable clutch-mechanism can be used for a more compact design and to achieve the same functionality (strategic coupling and decoupling).

When it comes to report structure, first, the research and reasoning behind the new actuator concept is introduced. Further, modeling, alongside control and simulation, is presented. Afterward, details on the experimental prototype and some of the key results are provided. In Section 3 whole development process is explained. Finally, Section 4 details the mechatronic development aspect of the deliverable.

2 Investigation of the Actuator Concept

One of the main drawbacks of intrinsically elastic actuation is that the timing of energy storage and release cannot be fully controlled. For better control over the energy flow in the system, the robotics community has identified clutches in the drive-train as a possible remedy [7]. Depending on the use case and task at hand, clutches can be introduced in the actuator to bypass or lock elastic elements. Due to the large number of possible applications, there is also a large number of designs. These range from passive unilateral clutches, primarily used in prosthesis [9] to active bilateral clutches in a manipulation

context [10]. The resulting designs can also become very complex. For example, [11] uses several clutches and brakes to produce a wide range of behaviours. Out of the many different design options, we now had to systematically explore and find the right option for Darko. Our strategy was four-fold:

- i) Use simulation and optimal control to select the best concept.
- ii) Design a modular configurable testbed using off-the-shelf components that allows for the implementation of different clutch and brake options in combination with the SEA.
- iii) Implement and test the design using the modular testbed.
- iv) Based on the experiments, revise the design create a more compact version.

In this section, we now explain our approach to the optimal control study for design selection.

2.1 Concept Requirements

The purpose of the new clutch-mechanism is to give the Darko arm the ability to throw objects, which requires a high end-effector speed. Many concepts would meet this goal; even a simple SEA design without any clutches. Therefore, we further constrained our search space by another requirement that concerns the movement strategy itself: Instead of oscillatory swing-up motions, we required a clear launch-sequence – akin to human throwing or to launching a trebuchet (see Fig. 1).

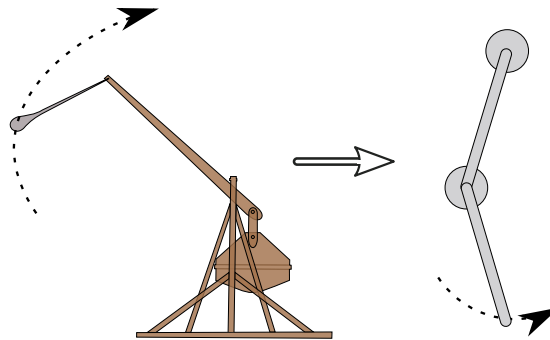


Figure 1: Design vision: By using a suitable clutch-mechanism, we have full control over the energy-transfer timing in an elastic robot arm – and can launch it similar to a trebuchet.

2.2 Concept selection

As a starting point for our concept, we consulted some previous work regarding optimal control for VSAs [2]. In this work, the speed of an elastic double pendulum equipped with VSAs is maximized at fixed final times. Here, for the specific case of small final times, VSA used approximate decoupling of the link from the actuator to maximize the energy transfer from proximal to distal joints – resulting in the proximo-distal sequence discussed earlier. For approximate decoupling, two main modes are required: A maximum stiffness setting and a very low stiffness setting.

These considerations led to a new actuator concept called *Bi-Stiffness Actuation* (BSA) [12]. It consists of a motor that is connected to a series spring element, which can be either coupled to the link side using a switch-and-hold mechanism, or locked to the fixed frame

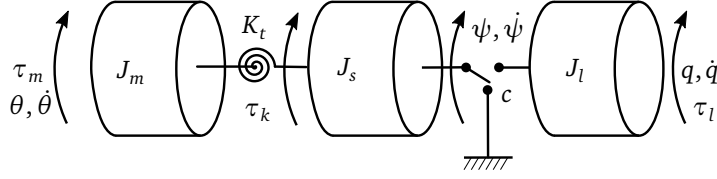


Figure 2: Sketch of the proposed actuator. The spring inertia can be locked in place, while the link is decoupled or connected directly to the link. We can therefore distinguish two distinct modes: The decoupled mode (DEC) and the series elastic actuator mode (SEA).

such that no potential energy is lost when the link is decoupled (see Fig. 2). The actuator can thus toggle between decoupling, i.e. zero stiffness, and the full stiffness mode, SEA, hence the name Bi-Stiffness.

2.3 Concept Verification

To verify that this concept meets our requirements (high speed plus clear launch-sequence), we conducted an optimal control study directly comparing our design against a VSA. From the start, we used a simulated double-pendulum as the means of comparison, since this represents the most simple system that encompasses the full nonlinear robot dynamics. Since two links need to be coordinated, this puts also the movement strategy of the actuator to a good test.

2.3.1 Modelling

The clutch action requires special attention when generating the robot model. Similar to the legged robot case [13], our robot can be modelled as a hybrid system. Introducing the vector of motor θ , spring ψ and link positions \mathbf{q} and defining $\xi := [\psi, \mathbf{q}]^T$, the equations of motion of a robot actuated by BSA can be obtained¹:

$$\underbrace{\begin{bmatrix} \mathbf{B} & \mathbf{0} \\ \mathbf{0} & \mathbf{M}(\mathbf{q}) \end{bmatrix}}_{=: \mathbf{\Pi}(\xi)} \ddot{\xi} + \underbrace{\begin{bmatrix} \mathbf{0} \\ \mathbf{h}(\mathbf{q}, \dot{\mathbf{q}}) \end{bmatrix}}_{=: \boldsymbol{\eta}(\xi, \dot{\xi})} + \underbrace{\begin{bmatrix} \mathbf{K}(\theta - \psi) \\ \mathbf{0} \end{bmatrix}}_{=: \boldsymbol{\tau}_k} = \mathbf{C}_p^T \boldsymbol{\lambda}, \quad (1)$$

$$\mathbf{C}_p \dot{\xi} = \mathbf{0}. \quad (2)$$

Here, $\mathbf{B} = \text{diag}(J_{s,1} \dots J_{s,n})$ denotes the spring inertia matrix, where n is the number of DoFs, \mathbf{M} denotes the link-side mass matrix \mathbf{h} denotes the nonlinear bias term and \mathbf{K} denotes the stiffness matrix. Clutches restrict relative motion between two frames, which can be expressed as bilateral constraints (2). The different contact situations are encoded in matrices \mathbf{C}_p , where p is the current mode. The Lagrange multipliers $\boldsymbol{\lambda}$ that ensure the constraints are met (i.e. the constraint torques), can be computed in closed form from the constraint equation

$$\boldsymbol{\lambda} = (\mathbf{C}_p \mathbf{\Pi}^{-1} \mathbf{C}_p^T)^{-1} \mathbf{C}_p \mathbf{\Pi}^{-1} (\boldsymbol{\tau}_k + \boldsymbol{\eta}). \quad (3)$$

¹We state the dynamics in singular perturbation form, which leads to a simplified motor dynamics with $\dot{\theta}$ as the new control input. For details please refer to [12].

This leads to vector fields such that

$$\dot{\mathbf{x}} = \mathbf{f}_p(\mathbf{x}, \mathbf{u}) := \begin{bmatrix} \mathbf{u} \\ \dot{\xi} \\ \mathbf{\Pi}^{-1}(\mathbf{C}_p^\top \lambda - \eta - \tau_k) \end{bmatrix}, \quad (4)$$

where $\mathbf{x} := [\theta, \xi, \dot{\xi}]^\top$ and \mathbf{u} are the robot state and control input. For details, we refer the reader to [12]. Transitions between modes are modelled using a so-called *guard function* \mathbf{g}_p , which corresponds to an impulse upon the transition and ensures that the constraints after the impulse are fulfilled:

$$\mathbf{x}^+(t) = \mathbf{g}_p(\mathbf{x}^-(t)). \quad (5)$$

Here, \mathbf{x}^\pm corresponds to the state right before or after the impulse, respectively. The impulse can be expressed as an instantaneous update of the velocities

$$\begin{aligned} \dot{\xi}^+ &= \dot{\xi}^- + \mathbf{\Pi}^{-1} \mathbf{C}_p^\top \mathbf{\Lambda}_p, \\ \mathbf{\Lambda}_p &= -(\mathbf{C}_p \mathbf{\Pi}^{-1} \mathbf{C}_p^\top)^{-1} \mathbf{C}_p \dot{\xi}^-, \end{aligned} \quad (6)$$

which leads to

$$\mathbf{x}^+ = \mathbf{g}_p(\mathbf{x}^-) := \begin{bmatrix} \theta^- \\ \xi^- \\ \dot{\xi}^- + \mathbf{\Pi}^{-1} \mathbf{C}_p^\top \mathbf{\Lambda}_p \end{bmatrix}. \quad (7)$$

2.3.2 Optimal Control

With the model in place, an objective function $\mathcal{J}(\mathbf{x}(t), \mathbf{u}(t))$ (corresponding to the end-effector velocity at the final time, for example) can be minimized using a multiple-stage optimization problem

$$\begin{aligned} & \min_{\mathbf{x}(t), \mathbf{u}(t), T_p} \mathcal{J}(\mathbf{x}(t), \mathbf{u}(t)) \\ \text{s.t. } & \dot{\mathbf{x}}(t) = \mathbf{f}_p(\mathbf{x}(t), \mathbf{u}(t)), \quad t \leq T_p \\ & \mathbf{x}^+(t) = \mathbf{g}_p(\mathbf{x}^-(t)), \quad t = T_p \\ & \mathbf{x}(t) \in \mathcal{X}, \quad \mathbf{u}(t) \in \mathcal{U}, \end{aligned} \quad (8)$$

where the time-series of states and control inputs as well as the duration of each mode T_p are optimized. Additionally, the solution is restricted to constraint sets for state and control inputs \mathcal{X}, \mathcal{U} .

2.3.3 Simulation Results

We ensured that the systems actuated by BSA or VSA are power-equivalent. In the first experiment, the final time was fixed and the speed was maximized. Both systems were able to reach similar end-effector speeds at the final time, while drawing similar amounts of power, thus fulfilling the first design requirement. Next, we fixed the final speed and varied the final-times to see which kind of strategy the systems would employ. The main result can be seen in Fig. 3. BSA is able to consistently produce clear launch sequences (i.e. built-up of potential energy, then release). For a small final time, VSA is able to do the same, however, as the final time increases, resonant excitation becomes the prevalent strategy.

This study confirmed that with our new design, the energy transfer becomes intuitively controllable while reaching similar performance in comparison to a power-equivalent

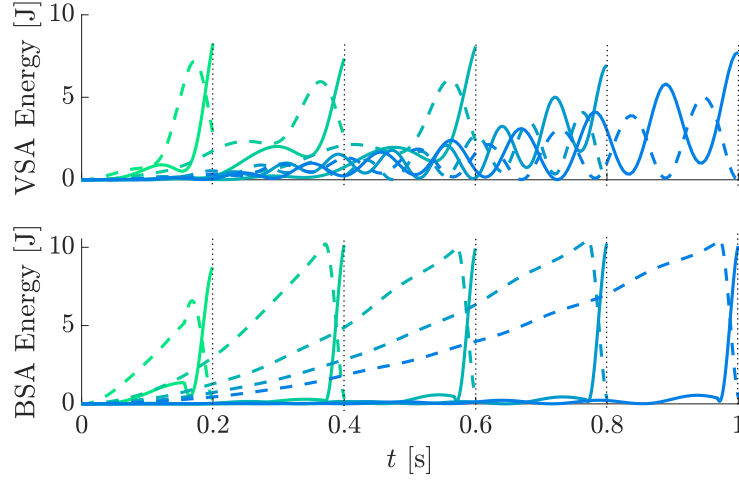


Figure 3: Total potential (dashed) and kinetic energy (solid) for different final times $t_f = 0.2 \dots 1$ s (indicated by color gradient from green to blue).

VSA. Next, we will present the development of our modular testbed [14], depicted in Fig.4(a)-(b). This was designed and implemented in parallel to our theoretical work in order to validate and test our new proposed concepts.

2.4 Concept Implementation

The immediate step after the concept validation was the introduction of a physical prototype of the actuator concept suggested in [12] as a 1-DoF physical system in order to fully validate our concept. In [14], we developed a configurable modular testbed by replacing the abstract switch-and-hold mechanism and interpret it as two individual clutches (see Fig. 4(c)), defining a new BSA architecture. Each module, except the motor, can potentially be connected in any permutation. This allows for the implementation of the BSA or SEA configuration. A summarized description is presented here, however, a comprehensive description of the hardware can be found in [14].

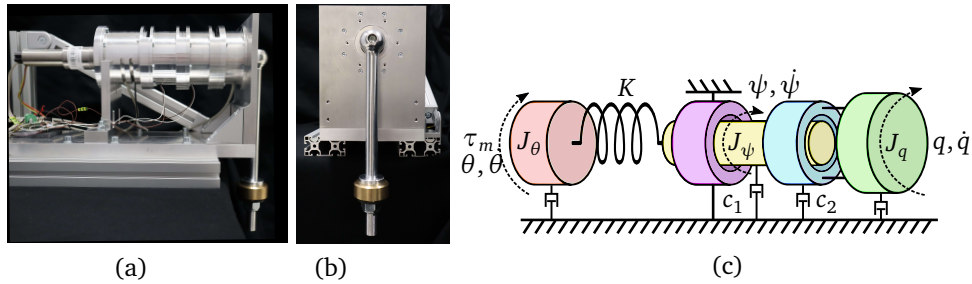


Figure 4: (a) Side-view and (b) Front view of the implemented BSA testbed. (c) BSA system model. The motor (red) is connected to the spring inertia (yellow), which can be either braked (violet clutch) or connected to the link (green) by the cyan clutch.

2.4.1 Architecture and Mechanical Design

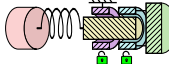
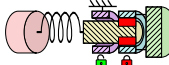
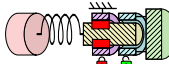
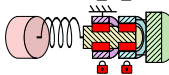
In the design process, we focused on two main paradigms: 1) Maximum modularity, and 2) Use of off-the-shelf components. The system is comprised of five types of modules: Motor (\mathbb{M}^M), spring (\mathbb{S}^M), brake (\mathbb{B}^M), clutch (\mathbb{C}^M), and link (\mathbb{L}^M). All modules are

designed with compatible a^f, b^f, c^f inputs and a^m, b^m, c^m outputs, where the superscripts f and m denote a female and male connection, respectively. In the following, we will provide a small description of each module.

- \mathbb{M}^M consist of a BLDC motor (Faulhaber GmbH, Germany) with a magnetic multi-turn absolute encoder and a 1:108 planetary gearbox and a manufactured adapter part to connect to the rigid frame of the other modules. The module has an a^m -type output.
- \mathbb{S}^M consists of an inner body with two inputs (a^f and b^f) and one output shaft (a^m) that contains a rotational spring based on Tsagarakis et al. [15] (See Fig. 2(a).), an embedded absolute magnetic encoder and a torque sensor. The advantage of this design lies in the use of off-the-shelf linear springs allowing the implementation of multiple stiffnesses.
- \mathbb{B}^M and \mathbb{C}^M are developed using a normally disengaged tooth clutch, each. On \mathbb{B}^M , the clutch has a rigid connection between its a^f input and a^m output shafts and toggles a connection to the outer frame of the module, braking and releasing the system, while the clutch in \mathbb{C}^M toggles the connection of its b^m output to its rigid connection between the a^f input and a^m output shafts.
- \mathbb{L}^M consists of a series of cross-roller bearings and an embedded absolute magnetic encoder. Its b^f input is connected to its c^m output and its a^f input is connected to a free-running bearing. \mathbb{L}^M can also be assembled to have its a^f input rigidly connected to its output too, providing some additional flexibility in possible future developments.

To assemble a BSA configuration, a permutation of \mathbb{M}^M - \mathbb{S}^M - \mathbb{B}^M - \mathbb{C}^M - \mathbb{L}^M is combined as depicted in Fig. 5.(a)-(b). The section view of the CAD assembly can be seen in Fig. 5.(b). The replacement of the switch-and-hold mechanism by the \mathbb{B}^M and \mathbb{C}^M adds two additional modes compared to the system introduced in [12] given that both clutches can be active or inactive at the same time. The new operational modes are summarized in Tab. 1.

Table 1: Actuator modes. If $c_i = 1$ the clutch is engaged, else if $c_i = 0$ it is disengaged.

Mode	c_1	c_2	
DEC (Decoupled)	0	0	
SEA	0	1	
STG (Storage)	1	0	
BRK (Braked Storage)	1	1	

2.4.2 Electronics and Control

The software, electronics, and control architecture are depicted in Fig. 5(c)-(e).

Main Controller. For quick employment of our optimal controllers, we use an EtherCAT framework (cf. Fig. 5(c)). A control PC hosts the high-level control routine using a Matlab / Simulink environment (MathWorks, MA, USA). It also hosts an EtherCAT master controller using Etherlab (Ingenieurgesellschaft IgH, Germany) at 1 kHz, including the submodule for interfacing the EtherCAT slave devices (ESD).

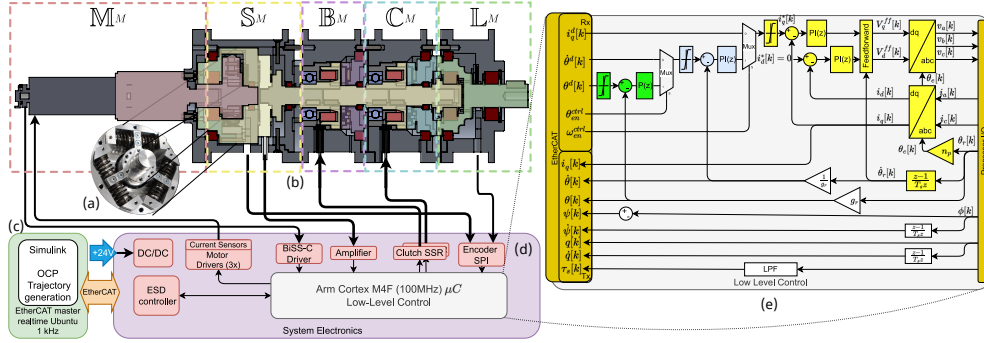


Figure 5: Detailed design of the implemented configurable modular testbed in BSA configuration (M^M - S^M - B^M - C^M - L^M). (a) Designed spring element. (b) Section-view of CAD assembly. (c) PC-based main controller. (d) Custom-made electronics. (e) Low-level Cascaded Controller.

Embedded Controller Hardware. To reduce the electronic footprint, we developed a custom low-level slave device subsystem, composed of a custom-made embedded brushless DC motor controller board, as shown in Fig. 5(d). It is based on an ARM Cortex-M4F microcontroller (μC) with a single-precision floating-point unit (FPU) running at 100 MHz. Two current sensors are located in line to phases A and C of the motor and connected to the two analogue-to-digital converters (ADC) to read currents i_a and i_c , respectively. A strain gauge Wheatstone full-bridge torque sensor differential amplifier circuit is also connected to the ADC to read τ_s from S^M . One Serial-Peripheral-Interface (SPI) bus is used to communicate with the magnetic encoders and read ϕ and q from S^M and L^M , respectively, and an additional SPI bus with a BiSS-C transceiver is used to receive data from the BLDC rotor position, θ_r . Both the ADCs and SPI modules are synchronized with the Pulse Width Modulation (PWM) module used for driving the motor via three half-Bridge inverters at 12.5 kHz. Additionally, two digital channels are provided to turn on/off the clutch/brake actuators using solid state relays (SSR). The system also comprises a real-time EtherCAT-based slave communication sub-module running at 1 kHz using a LAN9253 slave controller.

Embedded Controller Firmware. Within the μC , a programmable multilevel cascaded controller runs and controls the actuators as shown in Fig. 5(e). This controller provides ease of use for presetting modes (e.g. initial position adjustment, calibration, etc.) or running modes such as those required by our optimal control trajectory generator. The inner loop (yellow) runs a current controller using PI-based Field Oriented Control [16], the middle loop (cyan) is a PI-based speed controller with anti-windup, and the outer loop (green) is P-based position control. Three discrete estimators are used to estimate $\hat{\theta}_r$, \hat{q} , and $\hat{\psi}$. A low pass filter (LPF) is also implemented to filter the acquired τ_s signal. θ and $\dot{\theta}$ are calculated using the gearbox ratio g_r , of M^M . All control parameters, proportional and integral gains, cut-off frequency, etc. are sent to the system from the main controller via the EtherCAT bus. Both the outer and middle loops can be bypassed with θ_{en}^{ctrl} and $\dot{\theta}_{en}^{ctrl}$, respectively. the system can be controlled by an external reference signal via the EtherCAT bus when required. All measured and estimated variables such as θ , $\dot{\theta}$, q , \dot{q} , ψ , $\dot{\psi}$, i_q , τ , etc. are provided to the main controller via the EtherCAT bus.

2.4.3 Experimental Results

We conducted a series of experiments that compared the performance of the prototype in both SEA and BSA modes in order to assess the concept performance. These experiments

involve solving an optimal control problem (OCP), whose details can be followed up in [14].

The initial set of experiments evaluate explosive motion capabilities of the actuator. Starting from equilibrium at $\xi = 0$, the trajectories are optimized to maximize the link velocity \dot{q} within fixed final times t_f . The sequence BRK \rightarrow SEA is encoded in the optimization so that the spring can be loaded with maximum speed. Some time after, the brake is released, and the motor works in liaison with the spring to first accelerate in one direction. The stored potential energy is quickly transformed into kinetic energy. Then, the motor changes direction, essentially doing a single "bang". On the other hand, using only the SEA mode, the actuator employs a resonant excitation strategy using a bang-bang-like signal which is typically associated with this type of actuator [3].

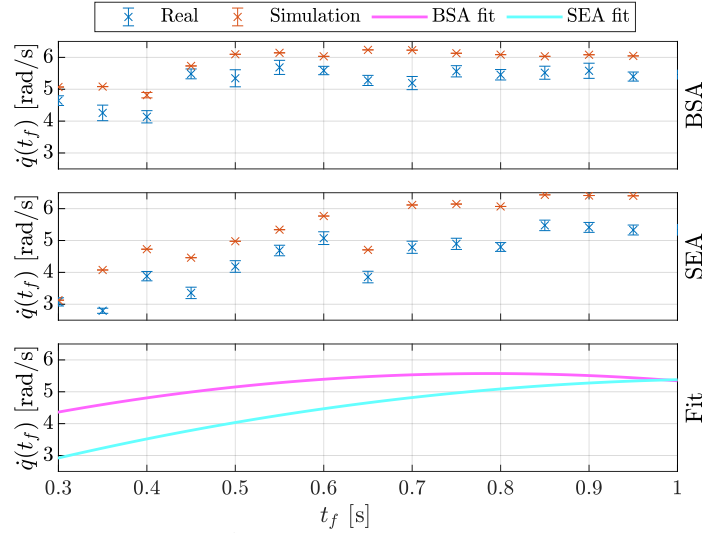


Figure 6: Statistical evaluation of the *Maximization of \dot{q} for varying final times t_f* experiment. The acquired data from the system (blue) and the online simulation data (red) are shown for the BSA (top) and SEA (middle) cases. A polynomial fit (bottom) of the mean velocities of the experimental data is shown.

Fig. 6 depicts the results from the statistical evaluation. The plot illustrates the mean and standard deviation for both the actual system (blue) and online simulation (red). Each t_f experiment is repeated 10 times. Consistently, for $t_f > 0.45$ s, BSA achieves final velocities above $\dot{q} = 5$ rad/s. While maintaining good performance at higher t_f values, SEA falls short in achieving comparable velocities at small t_f . Notably, for $t_f < 0.4$ s, the BSA solutions lack time for bidirectional acceleration (previous "single bang"), leading to slightly lower final \dot{q} . For optimal SEA performance, the resonance frequency of the system would have to be aligned with the designated time window by selecting the appropriate stiffness value. Although it would excel in this specific combination, its performance would be less satisfactory for every other time window.

By examining the kinetic (E_k) and potential (E_p) energy evolution of BSA and SEA at $t_f = \{0.3, 0.7, 1\}$ s, as depicted in Fig. 7, we can see how the BSA generates consistent launch sequences (slow build-up and rapid release). When examining SEA signals, potential and kinetic energy oscillate for all end times, indicating resonant excitation.

In the latter set of experiments, we focused on maximizing the link velocity, but starting from an inclined angle $q_0 = 10 \dots 50$ deg. We calculated the optimal trajectories delimiting a free end-time $t_f \in [0 \dots 0.5]$ s and repeated each trajectory 10 times.

Our results show that as a BSA, the system while in STG mode, decouples the link and locks the spring. The motor loads the spring while the link is accelerated by gravity alone.

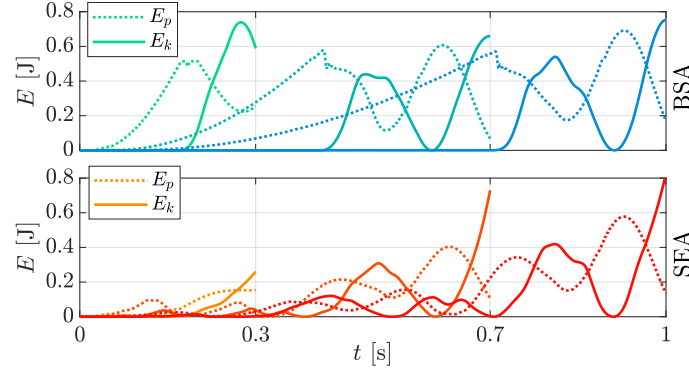


Figure 7: Evolution of the potential E_p and kinetic E_k energy for the *Maximization of \dot{q}* for varying final times t_f experiment. The plots are the superimposed cases of $t_f = \{0.3, 0.7, 1\}$ s.

After some time, the mode is changed to SEA and the stored potential energy is converted to kinetic energy, further accelerating the link. In the SEA case, the motor moves with the link, however it cannot contribute much to accelerate it. This becomes also evident when viewing the spring deflection ϕ , whose magnitude is relatively low compared to the BSA case. In Fig. 8, the reached end velocity is plotted against the initial positions q_0 . With increasing joint initial positions, the BSA also proportionally outperforms the SEA in terms of end velocity, exploiting the aforementioned synchronicity effect. With the BSA's decoupling capability, we are not only able to precisely time the release of joint potential energy but also synchronize its release with the gravity potential.

Therefore, these experiments confirm that with a BSA, we can control the timing of energy storage and release; and reach a higher end-velocity in shorter periods of time while also avoiding resonant excitations with lengthy swing-up motions.

3 Development Strategy and Stages of the Deliverable

Given the complexity of the deliverable and the limited development time, a full strategy was developed after the initial results from the development of the modular testbed. This strategy, shown in Fig. 9, is divided in two main branches: Control and Mechatronics among four stages. This split allows the distribution of the main tasks among our team members based on their expertise, while maintaining a high level of communication among them.

The timeplan of the development can be seen in the Figure 10.

3.1 Stage 1

This stage refers to the preliminary work explained in Section 2.4.1. As previously mentioned, the developed worked not only allowed us to validate the BSA principle but also provided us with a configurable testbed for easy initial prototyping.

Modelling, Simulation and Optimal Control This block enclosed to the work developed in [12].

Configurable Modular 1-DoF Joint This block refers to the configurable testbed developed in [14] and the modifications to the modelling and Optimal Control of the 1-DoF BSA.

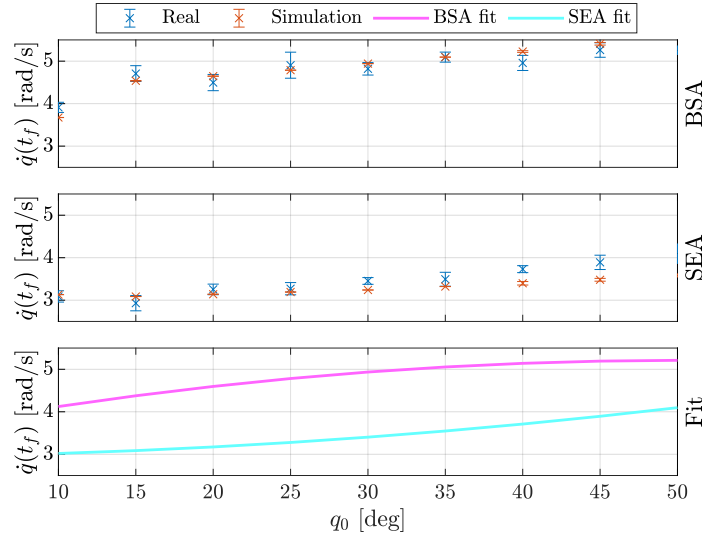


Figure 8: Statistical evaluation of the *Maximization of \dot{q} for varying initial position q_0* experiment. The acquired data from the system (blue) and the online simulation data (red) is shown for the BSA (top) and SEA (middle) cases. A polynomial fit (bottom) of the mean velocities of the experimental data is shown.

3.2 Stage 2

This stage comprises the follow up work from the preliminary results. As stated, the team work is divided in two paths in order to achieve good results.

Modular 2-DoF BSA prototype This main block focuses on the implementation of a 2-DoF BSA prototype with an inverted pendulum configuration, a preliminary architecture to the 3 DoF Manipulator. With the use of the modular testbed, a fast prototype can be achieved. With this new prototype, further development can be performed on the required optimal control strategies to achieve a robust system performance and to evaluate scenarios that do not occur on the 1-DoF system. This block has two sub-modules that are required to be identified:

- **Modelling & Simulation** This sub module emphasises the required changes and adaptation of previously developed BSA models to the new 2-DoF BSA inverted pendulum prototype.
- **Contact Implicit Optimal Control** The focus of this sub-module is further development of the Optimal Control solutions. In previous work, the mode change of the BSA actuator is considered to be known apriory (intuitive guess). However, this approach might not lead to the true optimal solution. Thus, the optimal control problem should be reformulated such that the mode switching sequence will be determined by the optimizer itself. That is particularly evident, now that two BSA actuators are present. With the increase of the BSA actuators number, it's getting harder to provide a valid guess for the switching sequence.
- **LQR** This sub-block focuses on the implementation and testing of a Linear Quadratic Regulator (LQR) in order to achieve a closed-loop control of the 2-DoF System. Closed-loop control is particularly useful to achieve more trajectory tracking by overcoming non-modeled system nonlinearities.

On the other path, the team focused on the developed of required components in order

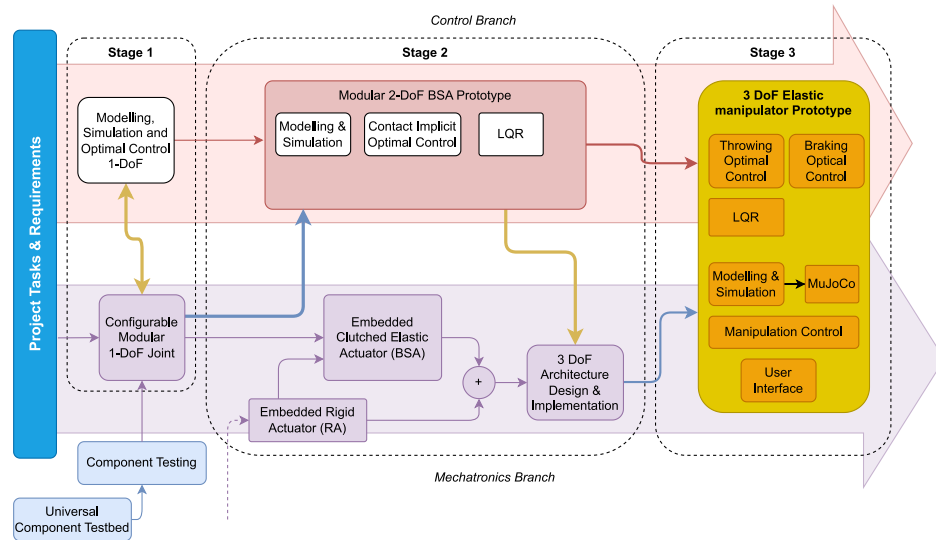


Figure 9: Strategy of Manipulator development within DARKO project.

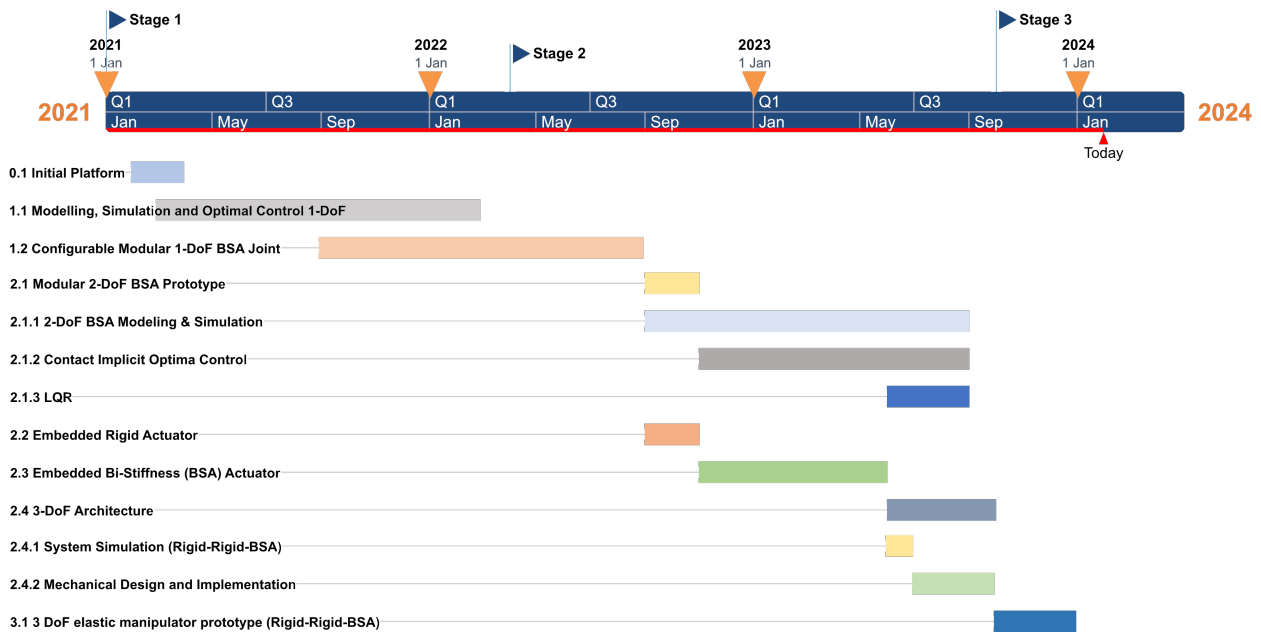


Figure 10: Timeline of 3DoF development within DARKO project.

to build a proper 3DoF system.

Embedded Rigid Actuator Block focuses on the revision, selection and evaluation of a Rigid Actuator Design as an auxiliary actuator unit for the links of the manipulator that would not require a series elastic actuator.

Embedded Bi-Stiffness Actuator This block is comprised on the design, implementation and evaluation of an embedded actuator based on our previously validated BSA strategy.

This module includes: motor, gearbox and sensor selections, mechanical frame, mechanisms and assembly design, embedded torque sensor design; and electronics adaptation and design.

3 DoF Architecture Design This main block is comprised of the design and implementation of the manipulator architecture based on the previously developed actuators, control strategies and requirements (e.g. speeds, payloads, throwing trajectories, etc)

3.3 Stage 3

This stage is comprised on the implementation and testing of the mid-level control strategies developed for the 2-DoF system and extrapolated to the new architecture, as well as the systematic testing of the architecture and mechatronics.

3 DoF elastic manipulator prototype The development of the final manipulator is comprised, as mentioned, on many small stages dependant on previous blocks that require the effort of the full team, given the inter-twinned work, and thus, it is represented on both paths. Many of the previously developed block need to be migrated to the new architecture following the same methodology, and new blocks will be developed as part of the final system requirements.

4 Execution of the Strategy

4.1 Modular 2-DoF BSA prototype

After successfully testing BSA's capability in an actual hardware prototype, a double pendulum 2-DoF BSA system is implemented as presented initially in [12]. The system consists of two configurable modular subsystems that correspond to the prototype presented previously. Figure 11 shows the new testbed and it's internal structure. J_2 utilizes a revised version with optimized weight. The torque sensors in both actuators have been upgraded to the ± 10 Nm range. Additionally, a rigid coupling mechanism is added between \mathbb{L}^M of J_1 and the ground frame of J_2 . The control PC runs the high-level real-time control as before, and transmit the data via the EthetCAT I/O interface using a series network topology. The optimal control trajectories are solved within the Matlab environment (outside the real-time system) and stored and used as look-up tables (LUTs).

4.1.1 Implementation and Results

For testing, we implemented a multi-stage optimization problem similar to (8). Additionally, we utilized a hybrid linear quadratic regulator similar to [17] for tracking the solution. The experimental results are depicted in Fig. 12.

Both actuators start in STG (Storage) mode. The spring in joint 1 is loaded with the maximum possible speed. The spring in joint 2 is also loaded at the same time at a slower speed due to the spring deflection limits. At $t = 0.22$ s, joint 1 switches to SEA mode and releases it's potential energy swinging link 1 forward. Link 2 is swung passively by joint 1. As link 1 reaches it's velocity maximum at $t = 0.42$ s, joint 2 also switches to SEA mode leading to the peak velocity at the final time of $t = 0.5$ s. This example precisely illustrates BSA's capability to realize a coordinated launch sequence similar to the proximo-distal sequence in biomechanics. It further illustrates that this also translates to a fully nonlinear 2 DoF physical prototype of the system which shows good tracking behaviour when a equipped with a suitable tracking controller.

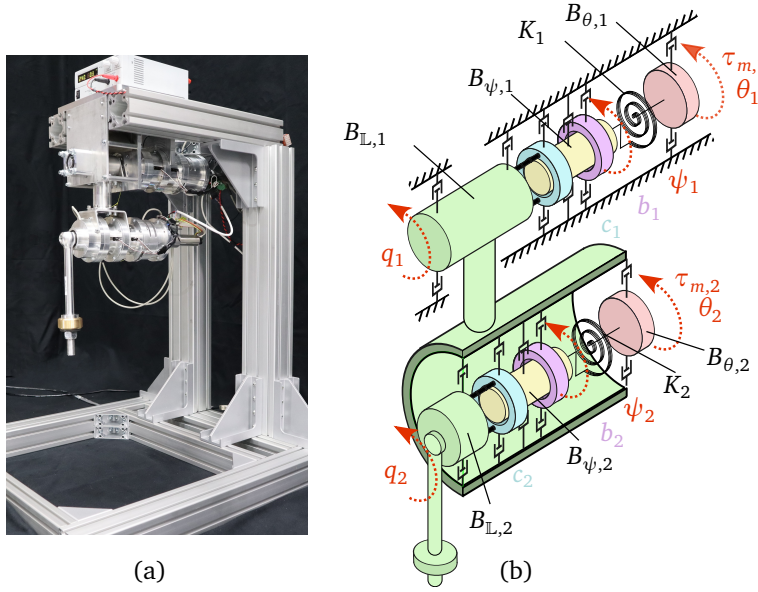


Figure 11: Hardware setup (a): Experimental 2 DoF elastic pendulum actuated by two Bi-Stiffness Actuators. Internal structure (b): For each joint J_i , the spring inertia can be locked in place by brake b_i (violet) and/or coupled directly to the link by clutch c_i (cyan).

4.2 Embedded Bi-Stiffness Actuator: (\mathbb{BSA}^b)

4.2.1 Preface: Embedded Rigid Actuator (RA)

We used the previously developed embedded rigid actuator from the "Prototype II - The ANP" Prosthesis by Toedtheide et al. [18] as a starting point for our designs. The previously achieved positive results from our institute's research and development were a key factor to point in the right direction of component selection. We also used this design as a supporting actuator model for the development of our elastic manipulator.

4.2.2 BSA Architecture

As stated previously, once the BSA concept was successfully verified, we proceeded to develop an new Bi-Stiffness actuator with the same properties in order to fully develop our elastic manipulator prototype. Some of the design requirements were set to 24V operational voltage, maximum joint angular speed of up to 10 rad/s, and a torque range of 20 Nm. One of the key aspects in the development was the reduction of the actuator mass in order to reduce the payload on the future robot. By reducing the modularity of the actuator, and with the replacement of key components, an integrated version of the actuator was achieved.

The \mathbb{BSA}^b is developed as two main modules: \mathbb{M}^e , an embedded CEA comprised of an SEA with a break; and \mathbb{C}^e , an embedded clutch module. This module-based design provides us more freedom in the design of the multi-DoF systems with different architectures. Some of the specifications are shown as follows:

- \mathbb{M}^e replaces the \mathbb{M}^M , \mathbb{S}^M and \mathbb{B}^M . It is designed using a stationary rigid spline hollow shaft adopted from the jet engine designs. All rotary elements are put along this spline and all wiring is send to the back via the like hollow channel. To achieve this architecture, the \mathbb{M}^m was replaced by a frameless brushless DC motor, a Harmonic Drive gear box

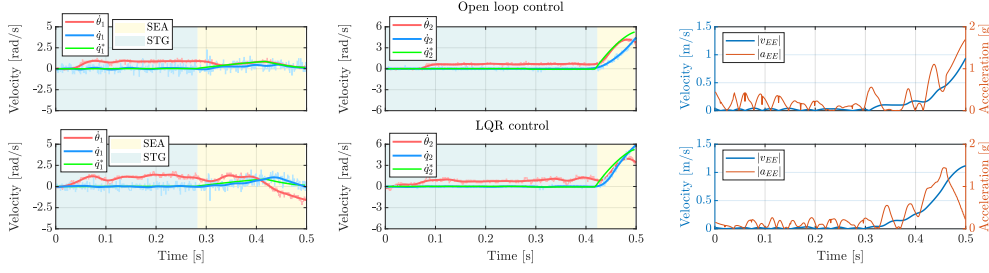


Figure 12: Experimental results - *Speed maximization at fixed final time*. The results, without and with the LQR controller, are presented in the upper and lower rows, respectively. The background color denotes the operating mode, with yellow representing SEA and turquoise indicating STG. The left and middle plots show the changes in motor angle $\theta_{1,2}$ (red) and link angle $q_{1,2}$ (blue) as raw and filtered data and the reference $q_{1,2}^*$. The plots were smoothed utilizing Matlab's smoothdata function. The plots on the right depict the magnitude of the end effector's velocity $|v_{EE}|$ (blue) and acceleration $|a_{EE}|$ (orange).

set and a Aksam 2 absolute magnetic encoder. To avoid the problem of the cumulative length of the integrated components as in the previous prototype, several parts are tried to place in parallel to each other. Thus, the S^M is replaced by a cage-like spring mechanism suggested by Sariyildiz et al. [19]. This caged like structure allow us to get a high deflection-to-maximum-torque ratio and embed the clutch from the B^M inside the spring as well. The on-board torque sensor was replaced by four strain-gauges installed in two of the spring beams and connected to a distribution PCB. Additionally, the cage-like elements architecture is design in an adjustable manner, so for joints with different requirements, different stiffness can be applied. The output element of the module can allocate either an end-element to act as a braked SEA (SEA-B) module, or a teathed rotor for the clutch element of the C^e block. The clutch element was not replaced by a new component due to availability, however, this leaves open for further improvements in our design.

- C^e substitutes the C^M and L^M . It is comprised of two cross-roller bearings, an embedded absolute magnetic encoder and the armature of the C^M module.

Two revisions of the system were developed along the project. Single DoF tests were performed with v0.1 and evaluated. This preliminary results were used and modifications were made to obtain v0.2, where the mass was further reduced and the assembly process and adaptability was made easier.

4.2.3 Electronics and Low-level Control

The software, electronics, and control architecture are kept as close to the previous model as possible, however, some components were replaced or added in order to make it compatible to the new design or add new functionality.

Main Controller The same EtherCAT master controller on simulink was used, however, the controller frequency was set to 5 kHz to increase the controller capabilities. This limit is due to the embedded hardware capabilities.

Embedded Controller Hardware. A revised version of our PCB with minor changes is used for this actuator. The key change is the addition of another connector and slave selector at the main SPI bus to read the new rotor encoder, while the additional SPI bus with a BiSS-C transceiver was removed from the device. Thus, the SPI bus handle three encoders instead of two.

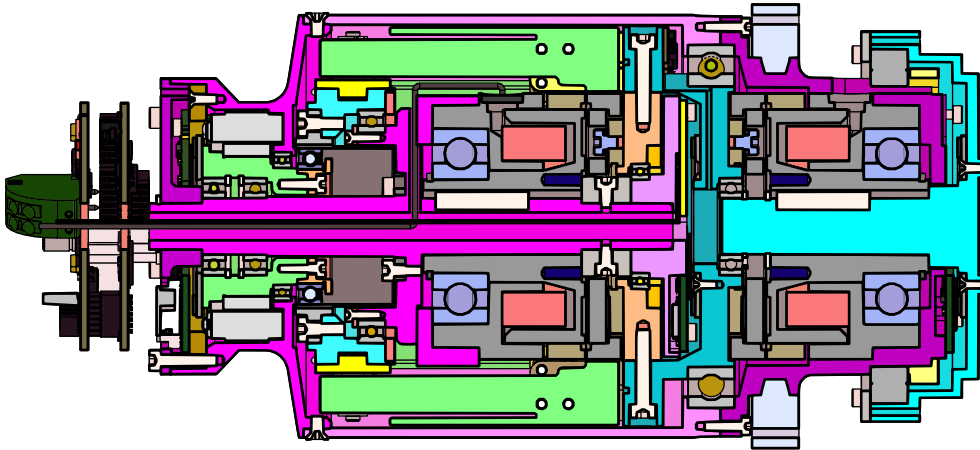


Figure 13: Section view of the $\text{BSA}_{v0.1}^b$ with mounted electronics (left).

Embedded Controller Firmware. Within the μC , the programmable multilevel cascaded controller that runs and controls the actuator was modified. An auxiliary torque P control loop (pink) was added in between the speed (cyan) and current loop (yellow). This additional loop can be turn on or by-passed. Additionally, the real-time EtherCAT-based slave communication sub-module was optimized to run at 5 kHz using the same LAN9253 controller.

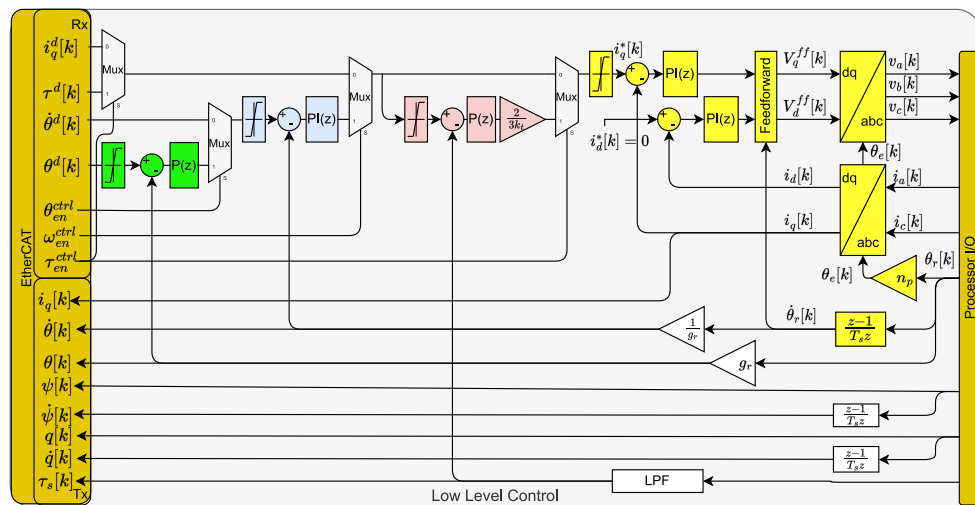


Figure 14: New low-level cascaded controller architecture

After the development of components and a preliminary platform, this stage is focused on in-depth components required to achieve a fully operational manipulator.

4.3 3 DoF Architecture

This main block is comprised of the design and implementation of the manipulator architecture based on the previously developed actuators, control strategies and requirements (e.g. speeds, payloads, throwing trajectories). One of the key elements for the development of our 3 DoF manipulator is the mechanical architecture of the system. This is comprised of the joint type selection for each of our DoF, their orientation within the structure and

the associated link dimension. The design and selection criteria are based on the main goal of the manipulator which is the maximization of the throwing speed of objects. Based on the selected parts for the Darko demo cases, a maximum payload of 0.3 kg was selected. Preliminary simulations were used to find the best structure for our manipulator based on the generated trajectories for throwing, which lead to the selection of Rigid-Rigid-BSA type of actuators with a yaw-pitch-pitch orientation: $RA^Y - RA^P - BSA^P$.

4.3.1 Preliminary Simulations

For selecting the architecture, simulation runs were conducted on a 3 DoF robot with permutations of rigid and BSA type joints. The permutation $RA^Y - RA^P - BSA^P$ already greatly outperforms a purely rigid robot. Despite limited motor speed of 2.5 rad/s, the robot reached a final cartesian velocity of 6.6213 m/s. Using the same motor speed limits, the rigid robot only reaches a cartesian velocity of 1.7 m/s. Fig. 15 shows the simulation run and Fig. 16 shows an animation. The first joint (yaw) performs a continuous movement and speeds up just before launch. The second joint (pitch) reaches its velocity maximum is released. Then, the third joint (pitch, BSA) decouples and is moved inertially by joint 2 and gravitational acceleration. This decoupling allows to effectively use gravity as an acceleration source surpassing the restrictions of the motor.

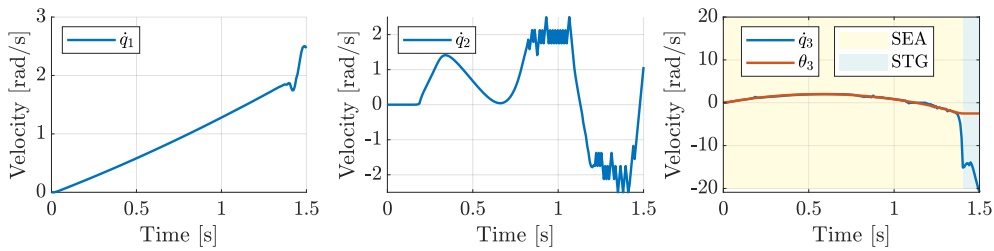


Figure 15: 3 DoF Simulation – *Speed maximization at fixed final time.*

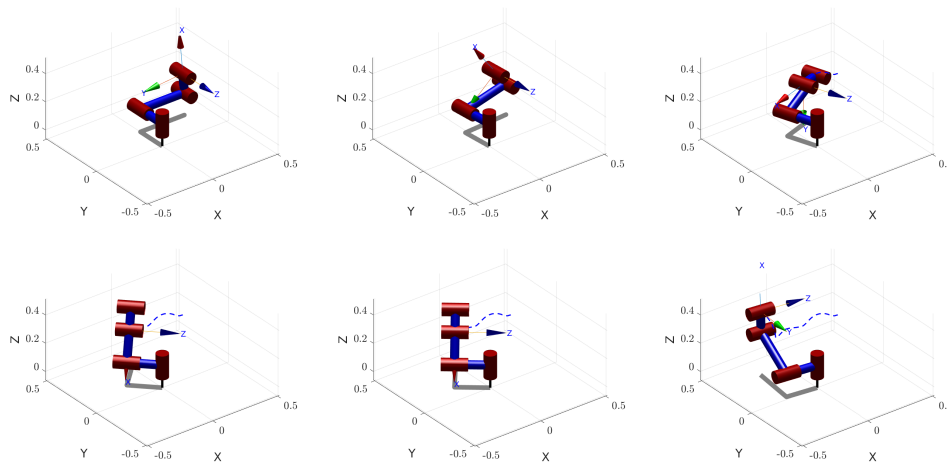


Figure 16: 3 DoF Animation – *Speed maximization at fixed final time.*

4.3.2 Mechanical Design and Implementation

Within our literature review, several strategies have been followed to increase the torque capacity of a robotic systems, such as parallel structures [20], cable and belt drive systems [21], counterbalance systems[22] etc. Due to the manipulation requirements of our system we decided to follow a counterbalance structure for our defined $RA^y - RA^p - BSA^p$. To further approve the usefulness of this strategy, we ran additional simulations with different center of mass (CoM) and mass distributions using the models of our RA and BSA components. The final distribution is shown in Fig. 17.

The initial joint, J_0 is placed in the center base of the robot with a yaw rotation and attached to the center of the initial link, l_1 . The second joint, J_1 is located in one side of l_1 and on the opposite side the second link l_2 is attached perpendicularly via its center using a cross-roller bearing. J_1 and l_2 are connected using a transmission beam. The BSA^b joint, J_2 is split in its sub-modules. M^e and C^e are located in opposite sides of l_2 and connected via a transmission belt. The final link l_3 is connected to the C^e output.

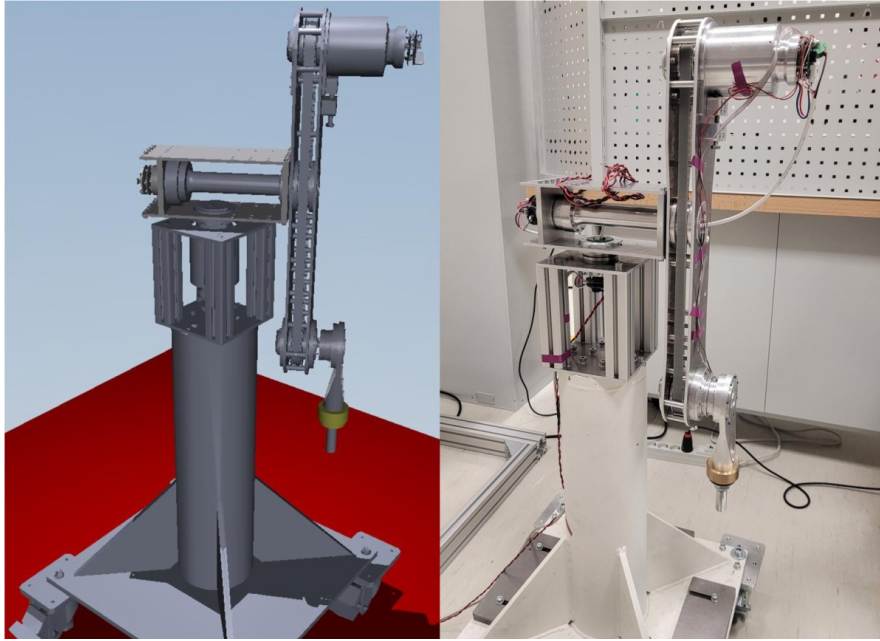


Figure 17: Picture of 3DoF arm prototype in MuJoCo simulation (left) and assembled (right) with configuration Rigid-Rigid-BSA.

This stage is comprised on the implementation and testing of the mid-level control strategies developed for the 2-DoF system and extrapolated to the new architecture, as well as the systematic testing of the architecture and mechatronics.

4.4 3 DoF elastic manipulator prototype

The development of the final manipulator is comprised, as mentioned, on many small stages dependant on previous blocks that require the effort of the full team, given the inter-twinned work, and thus, it is represented on both paths. Many of the previously developed block need to be migrated to the new architecture following the same methodology. Some new blocks are also developed as part of the final system requirements.

4.4.1 MuJoCo Simulation

MuJoCo simulation was developed to allow partners to easily try out and get to understand better various aspects of our mechatronic concept. 3DoF is modeled using dynamics described in Eq. 1. The Lagrange multipliers λ are added as external forces to the MuJoCo model, and calculated as stated in Eq. 3. Modes are encoded by C_p . In that way, closed-loop solution for λ will introduce contact forces in order to respect constraints specified in Eq. 2.

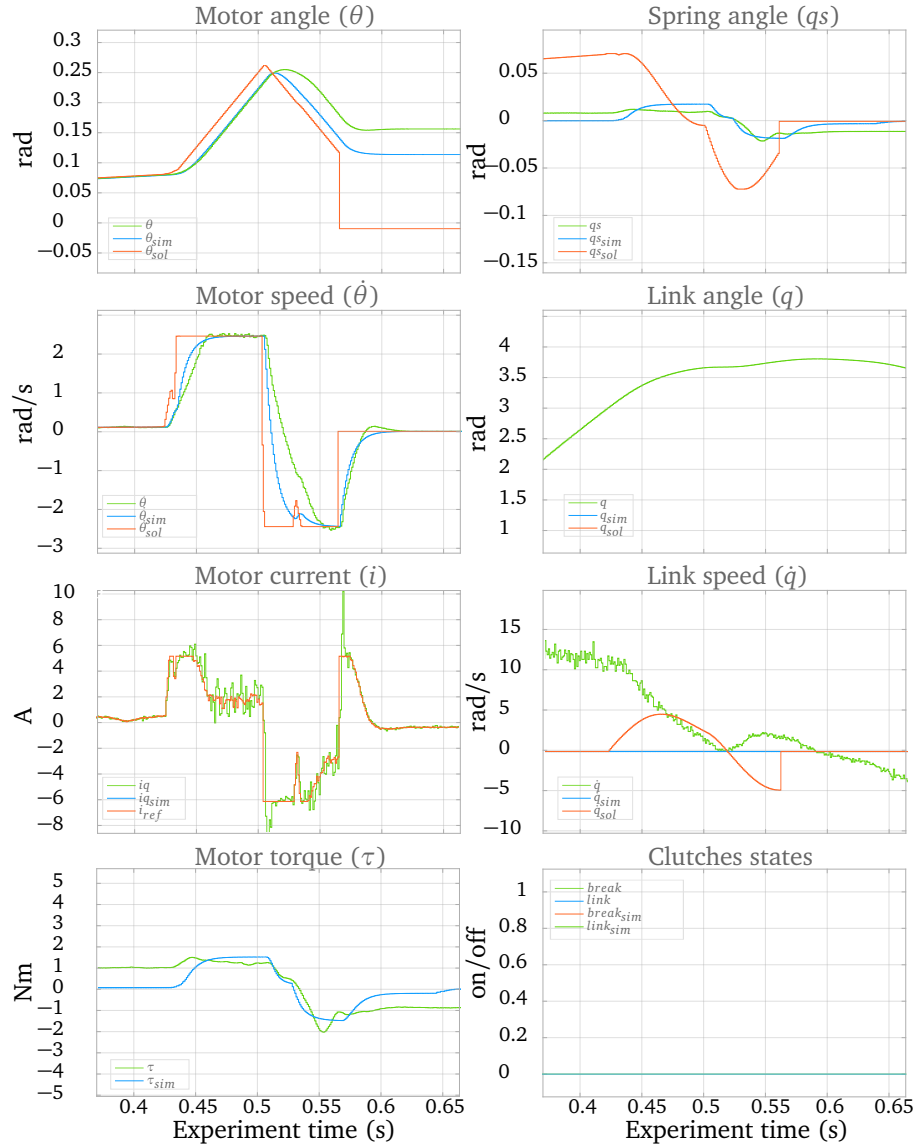


Figure 18: Testing reaction on fast change of speed reference from 2.5rad/s to -2.5rad/s on joint 2 (integrated BSA joint). In this case, the actuator is experiencing no external load, due to the ability of BSA to decouple the link from the motor and spring. Data represented in green is the data being read from the actuator.

4.4.2 Experiments

Short experiments are performed to show the individual actuator capabilities. In Figure 18, one can observe bang-bang speed test response of the actuator (tracking fast change of speed: $+2.5\text{rad/s}$ to -2.5rad/s). It can be considered as good indicator of capabilities, in particular, due to a showcase of low-level Current controller performance. Same test for rigid joints gives slightly different results depicted in Figures 19 and 20. Mostly due to always present inertia of connected joints. When tested prior to system integration (without inertia of connected links and joints), the performance of integrated BSA and rigid joints were similar. Further work will be focusing on showing the capabilities of the system as a whole, its ability to store and timely release energy, thus generating significantly larger EE velocities in comparison to rigid or SEA robotic solutions.

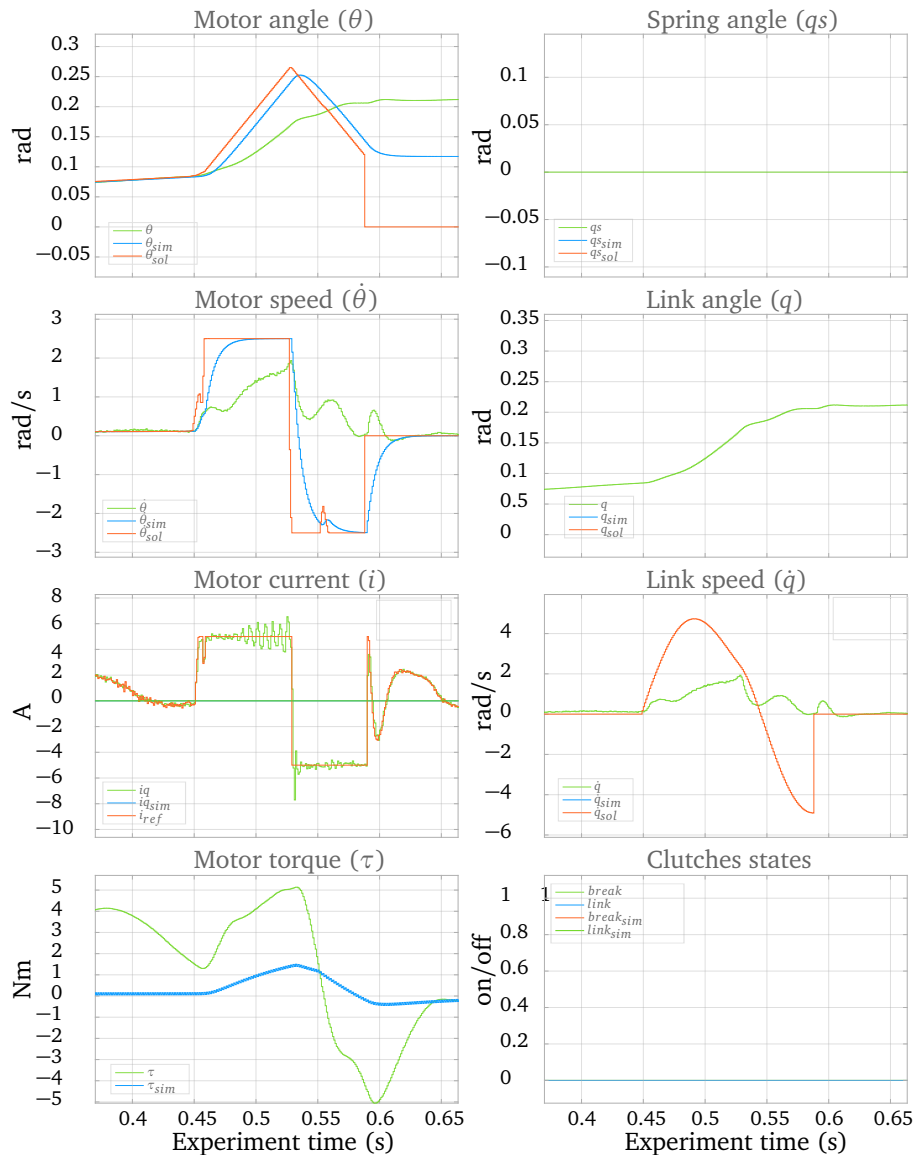


Figure 19: Testing reaction of joint 0 (rigid) on fast change of speed reference from 2.5rad/s to -2.5rad/s . Data represented in green is the data being read from the actuator.

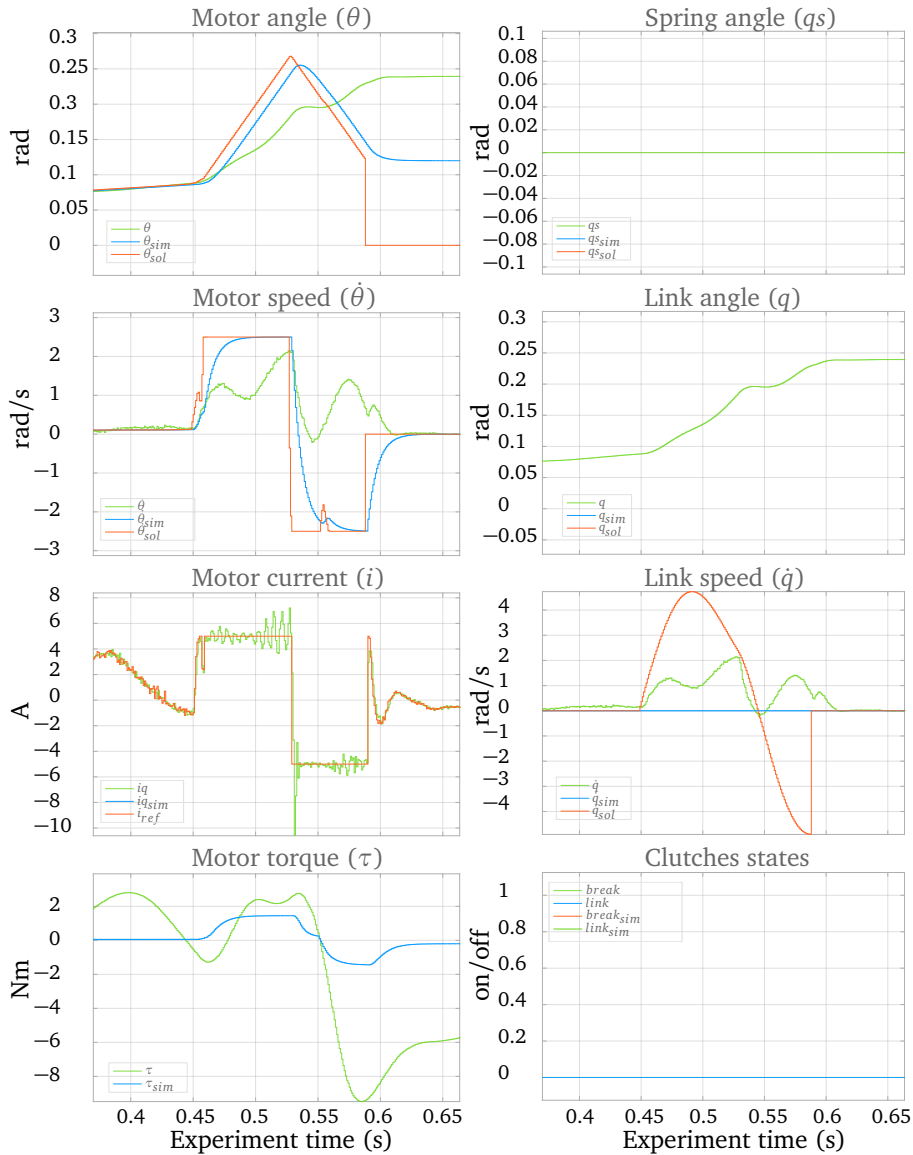


Figure 20: Testing reaction of joint 1 (rigid) on fast change of speed reference from 2.5rad/s to -2.5rad/s . Data represented in green is the data being read from the actuator.

5 Discussion

Within this deliverable a whole process and reasoning, alongside the results for an efficient throwing manipulator, was presented. It was argued and proven that to achieve the required milestone, combining existing solutions was not enough. The team needed to work on a whole new paradigm of actuation, named Bi-stiffness actuator. The concept was extensively tested and refined in simulation prior to its realization through mechatronic solution. The simulation was further refined for more accurate modeling of actuator dynamics. In 1DoF and 2DoF cases, a clear advantage was shown when it comes to the EE speed maximization. 3DoF is yet to prove the versatility of the solution for executing controlled throwing in different directions, keeping different goals in mind. Alongside providing manipulability comparable to state-of-the-art solutions.

References

- [1] *DARKO: Dynamic Agile Production Robots That Learn and Optimize Knowledge and Operations*. H2020 ICT-46-2020a: Research and Innovation Actions (RIA): Robotics Core Technology. Grant proposal. 2018.
- [2] Sami Haddadin, Felix Huber, Kai Krieger, Roman Weitschat, Alin Albu-Schäffer, Sebastian Wolf, Werner Friedl, Markus Grebenstein, Florian Petit, Jens Reinecke, et al. “Intrinsically elastic robots: The key to human like performance”. In: *Proc. 2012 IEEE/RSJ Int. Conf. on Intell. Robots and Syst.* 2012, pp. 4270–4271.
- [3] Sami Haddadin, Tim Laue, Udo Frese, Sebastian Wolf, Alin Albu-Schäffer, and Gerd Hirzinger. “Kick it with elasticity: Safety and performance in human–robot soccer”. In: *Robot. and Autonomous Syst.* 57.8 (2009), pp. 761–775.
- [4] Oliver Eiberger, Sami Haddadin, Michael Weis, Alin Albu-Schäffer, and Gerd Hirzinger. “On joint design with intrinsic variable compliance: derivation of the DLR QA-Joint”. In: *Proceedings 2010 IEEE International Conference on Robotics and Automation*. 2010, pp. 1687–1694.
- [5] Sebastian Wolf and Gerd Hirzinger. “A new variable stiffness design: Matching requirements of the next robot generation”. In: *2008 IEEE International Conference on Robotics and Automation*. 2008, pp. 1741–1746.
- [6] R. Van Ham, B. Vanderborght, M. Van Damme, B. Verrelst, and D. Lefeber. “MAC-CEPA: the mechanically adjustable compliance and controllable equilibrium position actuator for ‘controlled passive walking’”. In: *2006 IEEE International Conference on Robotics and Automation*. 2006, pp. 2195–2200.
- [7] Michiel Plooi, Wouter Wolfslag, and Martijn Wisse. “Clutched Elastic Actuators”. In: *IEEE Trans. Mechatron.* 22.2 (2017), pp. 739–750.
- [8] K Lehnertz. “Molekularmechanische Grundlagen der Muskelkraft bei Schlagbewegungen”. In: *Leistungssport* 5 (1984), pp. 27–34.
- [9] Elliott J Rouse, Luke M Mooney, and Hugh M Herr. “Clutchable series-elastic actuator: Implications for prosthetic knee design”. In: *the Int. J. of Robot. Research* 33.13 (2014), pp. 1611–1625.
- [10] Lisha Chen, Manolo Garabini, Matteo Laffranchi, Navvab Kashiri, Nikos G Tsagarakis, Antonio Bicchi, and Darwin G Caldwell. “Optimal control for maximizing velocity of the CompAct™ compliant actuator”. In: *2013 IEEE International Conference on Robotics and Automation*. IEEE. 2013, pp. 516–522.
- [11] Derek Leach, Fabian Günther, Nandan Maheshwari, and Fumiya Iida. “Linear Multimodal Actuation Through Discrete Coupling”. In: *IEEE/ASME Transactions on Mechatronics* 19.3 (2014), pp. 827–839.
- [12] Dennis Ossadnik, Mehmet C. Yildirim, Fan Wu, Abdalla Swikir, Hugo T. M. Kussaba, Saeed Abdolshah, and Sami Haddadin. “BSA - Bi-Stiffness Actuation for optimally exploiting intrinsic compliance and inertial coupling effects in elastic joint robots”. In: *Proc. 2022 IEEE/RSJ Int. Conf. on Intell. Robots and Syst. (IROS)*. 2022, pp. 3536–3543.
- [13] Dennis Ossadnik, Elisabeth Jensen, and Sami Haddadin. “Nonlinear stiffness allows passive dynamic hopping for one-legged robots with an upright trunk”. In: *2021 IEEE International Conference on Robotics and Automation (ICRA)*. IEEE. 2021, pp. 3047–3053.

- [14] Edmundo Pozo Fortunić, Mehmet C. Yildirim, Dennis Ossadnik, Abdalla Swikir, Saeed Abdolshah, and Sami Haddadin. “Optimally Controlling the Timing of Energy Transfer in Elastic Joints: Experimental Validation of the Bi-Stiffness Actuation Concept”. In: *IEEE Robotics and Automation Letters* 8.12 (2023), pp. 8106–8113.
- [15] N.G. Tsagarakis, Matteo Laffranchi, Bram Vanderborght, and D.G. Caldwell. “A compact soft actuator unit for small scale human friendly robots”. In: *Proc. 2009 IEEE Int. Conf. on Robot. and Autom.* 2009, pp. 4356–4362.
- [16] Edmundo Pozo Fortunić, Abdalla Swikir, Saeed Abdolsah, and Sami Haddadin. “Comparing Digital Implementations of Torque Control for BLDC Motors with Trapezoidal Back-Emf”. In: *Proc. 2022 Amer. Control Conf. (ACC)*. 2022, pp. 2546–2552.
- [17] Alessandro Saccon, Nathan Van De Wouw, and Henk Nijmeijer. “Sensitivity analysis of hybrid systems with state jumps with application to trajectory tracking”. In: *53rd IEEE Conference on Decision and Control*. IEEE. 2014, pp. 3065–3070.
- [18] Alexander Tödtheide. “Unified Force-Sensitive Robot Mechatronics”. en. PhD thesis. Technische Universität München, 2023, p. 164.
- [19] Emre Sariyildiz, Rahim Mutlu, Jon Roberts, Chin-Hsing Kuo, and Barkan Ugurlu. “Design and Control of a Novel Variable Stiffness Series Elastic Actuator”. In: *IEEE/ASME Transactions on Mechatronics* 28.3 (2023), pp. 1534–1545.
- [20] Mehmet C. Yildirim, Ahmet Talha Kansizoglu, Sinan Emre, Mustafa Derman, Sinan Coruk, Ahmed Fahmy Soliman, Polat Sendur, and Barkan Ugurlu. “Co-Ex: A Torque-Controllable Lower Body Exoskeleton for Dependable Human-Robot Co-existence”. In: *2019 IEEE 16th International Conference on Rehabilitation Robotics (ICORR)*. 2019, pp. 605–610.
- [21] D. Rodriguez-Cianca, C. Rodriguez-Guerrero, T. Verstraten, R. Jimenez-Fabian, B. Vanderborght, and D. Lefeber. “A Flexible shaft-driven Remote and Torsionally Compliant Actuator (RTCA) for wearable robots”. In: *Mechatronics* 59 (2019), pp. 178–188.
- [22] DongGyu Lee and TaeWon Seo. “Lightweight Multi-DOF Manipulator With Wire-Driven Gravity Compensation Mechanism”. In: *IEEE/ASME Transactions on Mechatronics* 22.3 (2017), pp. 1308–1314.



This project has received funding from the European Union's Horizon 2020 research and innovation programme under grant agreement No 101017274